

Hydrodynamic Inflation of Ring Polymers under Shear

M. Liebetreu ^{*1} and C. N. Likos ^{†1}

¹*Faculty of Physics, University of Vienna, Boltzmannngasse 5, A-1090 Vienna, Austria*

Abstract

Hydrodynamic interactions as modeled by Multi-Particle Collision Dynamics can dramatically influence the dynamics of fully flexible, ring-shaped polymers in ways not known for any other polymer architecture or topology. We show that steady shear leads to an inflation scenario exclusive to ring polymers, which depends not only on Weissenberg number but also on contour length of the ring. By analyzing velocity fields of the solvent around the polymer, we show the existence of a hydrodynamic pocket which allows the polymer to self-stabilize at a certain alignment angle to the flow axis. This self-induced stabilization is accompanied by transitioning of the ring to a non-Brownian particle and a cessation of tumbling. The ring swells significantly in the vorticity direction, and the horseshoe regions on the stretched and swollen ring are effectively locked in place relative to the ring's center-of-mass. The observed effect is exclusive to ring polymers and stems from an interplay between hydrodynamic interactions and topology. Furthermore, knots tied onto such rings can serve as additional "stabilization anchors". Under strong shear, the knotted section is pulled tight and remains well-localized while tank-treading from one horseshoe region to the opposite one in sudden bursts. We find knotted polymers of high contour length behave very similarly to unknotted rings of the same contour length, but small knotted rings feature a host of different configurations. We propose a filtering technique for rings and chains based on our observations and suggest that strong shear could be used to tighten knots on rings.

Introduction

The influence of topology on the physical properties of macromolecules is profound and manifold^[1]. The most striking manifestation of this fact is the vast richness of novel phenomena emerging in the behavior of ring polymers, both at the single-molecule level as well as for concentrated solutions and melts^[2–6]. Of immediate interest are, for example, the interplay between molecular architecture, deformation and dynamics under shear, but also how these affect stress distribution, viscosity, rheology and thixotropic behavior of sheared concentrated solutions. The conformations of single molecules and the ensuing effective interactions^[7–10], the self-organization of concentrated ring polymer solutions and melts^[11–17], the viscosity and stress relaxation under shear^[5,18–20] as well as the possibility of emergence of novel, topologically glassy states for ring polymer melts^[21–23] are a few characteristic examples of the variety of properties unique to cyclic polymers. Concomitantly, the out-of-equilibrium behavior of rings under tailored microfluidic flows has also attracted considerable attention in the recent past^[24–27].

As the probability to obtain unknotted polymers decreases exponentially with their contour length^[28], the importance of knots on polymer behavior is an additional topic of intensive research activity. Knots are naturally found on long DNA strands^[29–31] and proteins^[32–34] while at the same time they can also be artificially^[35,36] or synthetically manufactured^[37]. The influence of such knots

in equilibrium and relaxation properties in the bulk^[38–46], under confinement^[47–56] and under tension^[57–64] has been thoroughly investigated. Recently, the sedimentation behavior of flexible, non-Brownian knots has been added to the host of counterintuitive phenomena^[65].

All polymer architectures (linear, star, dendritic, cross-linked and ring) are known to undergo tumbling under steady shear at sufficiently high shear rates^[26,66–73]. Moreover, it is known that linear chains never fully stretch under shear and they reach a stretched configuration only under so-called planar mixed flows that represent a combination of simple shear and planar extension^[27,74,75]. Under simple shear, ring polymers show two dynamical modes: Tumbling (TB) and tank-treading (TT)^[76]. During TB, the polymer's shape changes rapidly as the ring collapses and expands again, with beads at the horseshoe regions swapping to the opposite side. The transition between initial and final state can best be described by the flipping of a disc, except it collapses onto itself during the flipping procedure. TT, on the other hand, is vastly different and becomes pronounced for stiff rings: the polymer ring maintains its shape, but beads start moving along its shape around the vorticity axis. This can best be visualized by a coin rolling on its edge, or the wheels of a tank.

In previous work, we have highlighted the importance of fully-developed hydrodynamics when investigating ring polymers under shear^[26]: Without rigidity, rings of sufficient length rarely show a pronounced TT motion, and short trefoil knots develop unique dynamics. Here, we present the emergence of an inflationary phase for ring polymers under simple, pure shear and fully-developed hy-

*maximilian.liebetreu@univie.ac.at

†christos.likos@univie.ac.at

hydrodynamic interactions caused by a backflow from the horseshoe regions. In this phase, the ring undergoes full unfolding in all directions and transforms itself to an almost rigid, stretched, non-Brownian particle, in which not only TT, but also TB motions are suppressed. The inflated regime is unique to ring polymers but independent of the presence of knots along their backbone but it requires a minimum polymer size to manifest itself. The aim of this work is to analyze the behavior of rings with and without knotted topology, and to quantify and explain the interplay between hydrodynamic interactions and topology. We suggest the swelling of the polymer in vorticity direction might potentially pave the way to distinguishing rings and chains of different sizes, and that shear could be used to reliably tighten knots on rings to unify the behavior of polymer melts. The vorticity swelling of all rings and its massive impact on dynamics and shape underlines the importance of fully-developed hydrodynamics when studying such polymers in solution.

Materials and Methods

We have employed Molecular Dynamics (MD) simulation coupled to a Multi-Particle Collision Dynamics (MPCD) solvent^[77], together with Lees-Edwards boundary conditions^[78], to simulate a variety of single ring polymers of various sizes and topologies under shear. In what follows, N stands for the number of beads in the polymer; the topologies simulated were the unknot, 0_1 , as well as the prime knots 3_1 , 4_1 , 5_1 , 5_2 , 6_1 , 6_2 , 6_3 , 7_1 and 8_1 , employing the Alexander-Briggs notation^[79] to characterize the knots.

Multi-Particle Collision Dynamics. The MPCD technique^[77,80] allows us to simulate a particle-based, mesoscopic solvent with fully-developed hydrodynamic interactions. MPCD features two alternating steps: streaming, where particles propagate, and collision, where one separates the system into smaller cells of length a and computes the center-of-mass velocity \mathbf{v}_{CM} in each, performing a random rotation of all deviations of the cell-particle velocity vectors from the latter, and adding it back to produce new, post-collision velocities. Because our simulations involve shear, the system would continuously heat up by viscous heating. To prevent this, we apply a cell-level Maxwellian thermostat^[81]. We employ the usual choice of parameters^[26,81–83] with a collision cell length a as a unit of length and rotation angle $\chi = 130^\circ$. All solvent particles are assigned a mass of m , serving as the unit of mass. We set the average number of solvent particles per cell as $\langle N_c \rangle = 10$ and the time step $h = 0.1 [(k_B T)^{-0.5} m^{0.5} a]$, with k_B being Boltzmann’s constant and T the absolute temperature. With our choice of parameters, the solvent dynamic viscosity η obtains the value^[81] $\eta = \eta_{kin} + \eta_{col} \cong 8.70 [(k_B T)^{0.5} m^{0.5} a^{-2}]$.

Lees-Edwards boundary conditions. The shear in our simulation is implemented by Lees-Edwards boundary conditions^[78] with a prescribed shear rate $\dot{\gamma}$. With $\hat{\mathbf{x}}$, $\hat{\mathbf{y}}$ and

Knot type	HI	N	$\tau_R [(k_B T)^{-0.5} m^{0.5} a]$
0_1	+	100	8543.84
0_1	+	150	15758.60
0_1	+	200	25902.20
3_1	+	100	5104.43
3_1	+	200	15874.20
4_1	+	200	13720.90
5_1	+	200	13219.00
5_2	+	200	13826.10
6_1	+	200	13404.70
6_2	+	200	12012.00
6_3	+	200	11673.50
7_1	+	200	13669.80
8_1	+	200	11394.30

Table 1. Relaxation times $\tau_R = a_0 \tau_1 + (1 - a_0) \tau_2$ for a variety of different knot types, partly at different contour lengths. a_0 , τ_1 and τ_2 are obtained from fitting $f(t) = a_0 \exp(-t/\tau_1) + (1 - a_0) \exp(-t/\tau_2)$ to the autocorrelation function $\Phi(t) = \langle \mathbf{R}_e(t) \cdot \mathbf{R}_e(0) \rangle / \langle \mathbf{R}_e^2 \rangle$.

$\hat{\mathbf{z}}$ being the flow, gradient and vorticity directions, respectively, these boundary conditions establish the velocity profile of planar Couette flow of the solvent in the absence of polymer as $\mathbf{v}_s(\mathbf{r}) = \dot{\gamma} y \hat{\mathbf{x}}$.

Molecular Dynamics. We employ the Kremer-Grest bead-spring model^[84,85] to investigate the properties of a fully-flexible polymer. We employ $\epsilon = k_B T = 1.0$ and $\sigma = a = 1.0$ as units of energy and length from the Weeks-Chandler-Andersen (WCA) potential, respectively. We set the parameters for the FENE potential to $k = 30 \epsilon \sigma^{-2}$ and $R_0 = 1.5 \sigma$. With these settings, the expected bond length $\langle l_b \rangle = 0.965 \sigma$. Velocity-Verlet^[86,87] with a time step $\delta t = h/100 = 0.001 [(k_B T)^{-0.5} m^{0.5} a]$ was used to solve the MD-equations of motion. This algorithm is easily coupled to MPCD by setting the mass of each monomer $M = m \langle N_c \rangle$ and having the monomers participate in the collision step^[26,81,83]. We have chosen to use the Alexander Polynomial^[88] to detect and the minimum-closure scheme to localize^[89] the knotted section on all simulated rings carrying knots. Simulating the various polymers in equilibrium allows us to determine as well their longest relaxation time τ_R , from which the Weissenberg number^[90] $Wi = \dot{\gamma} \tau_R$ can be extracted for different contour lengths. A summary of the relaxation times is given in Table 1.

GPU and system size. Our code has been written with CUDA/C++^[91] to run in parallel on a GPU cluster^[92]. This enabled more extensive simulations over a longer period of time to study flow profiles in detail. We also increased the simulation box volume to minimize residual effects by system size limitations. Our box sizes were $V = (100 \times 60 \times 60) a^3$ for a number of monomers $N = 100$ and $V = (150 \times 80 \times 80) a^3$ for $N = 150$ and $N = 200$. We have tested the influence of the box size by running a simulation with $V = (200 \times 120 \times 120) a^3$ for $N = 150$, which consistently reproduced the same behavior. Boxes are elongated in the flow direction $\hat{\mathbf{x}}$ to accommodate the

stretched polymer there, and quadratic in the gradient- and vorticity directions $\hat{\mathbf{y}}$ and $\hat{\mathbf{z}}$.

Results

Self-stabilization of long rings under shear and cessation of tumbling. Contrary to open-ended topologies like chains and stars, hydrodynamic interactions on rings cause the polymer to swell not only in flow, but also in the vorticity direction^[26]. To quantify the polymer's conformation under shear, we consider the gyration tensor^[93]:

$$G_{\alpha\beta} = \frac{1}{N} \sum_{i=1}^N \langle \mathbf{s}_{i,\alpha} \mathbf{s}_{i,\beta} \rangle, \quad (1)$$

where $\mathbf{s}_{i,\alpha}$ is the α -coordinate of particle i 's position relative to the polymer's center-of-mass $\bar{\mathbf{r}}$, such that $\mathbf{s}_i = \mathbf{r}_i - \bar{\mathbf{r}}$ and the symbol $\langle \dots \rangle$ denotes the expectation value arising from performing an averaging over time. The diagonal elements of this tensor express the polymer's extension in these directions and are shown in Fig. 1, plotted against increasing shear rate $\dot{\gamma}$. With the help of the results in Table 1, it can be established we have reached, for all polymers considered, Weissenberg numbers of order 10^3 , well into the strongly nonlinear regime, $Wi \gg 1$.

In flow direction (Fig. 1a), G_{xx} increases steadily up to a certain shear rate of approximately $\dot{\gamma} \sim 0.1$ and then it starts decreasing. Along the vorticity direction (Fig. 1b), G_{zz} experiences a short decrease and then increases rapidly up to a maximum before decreasing again. This effect is caused by backflow from the horseshoe regions of a stretched ring under shear and is exclusive to the ring topology^[26]. Already this non-monotonic behavior of the vorticity-direction diagonal component of the gyration tensor is quite unusual and unique to ring polymers but even more spectacular features show up in the gradient-direction diagonal element G_{yy} , shown in Fig. 1c. Contrary to all other known polymer types, which display a monotonic decrease of G_{yy} with the shear rate $\dot{\gamma}$, a swelling anomaly shows up for rings, resulting, for sufficiently long rings, in a non-monotonic behavior of G_{yy} and featuring a local minimum, a rise to a local maximum and a further decrease of this quantity thereafter. The effect is almost invisible for a contour length of $N = 100$, i.e., one needs sufficiently long rings to clearly identify it.

During the anomaly in the behavior of G_{yy} , the $N = 150$ and $N = 200$ rings undergo a shift in behavior, transitioning from the usual motion that features strong thermal fluctuations on the monomer scale as well as tumbling of the whole macromolecule, towards a new phase in which the ring is stretched and unfolded, and the tumbling motion stops. At the end of this phase, which takes place for shear rates bracketed by the local minimum and the local maximum of G_{yy} , the ring behaves as a non-Brownian particle for which thermal fluctuations are strongly suppressed by the strong hydrodynamic and elastic forces between connected monomers. Since this phase manifests itself as an

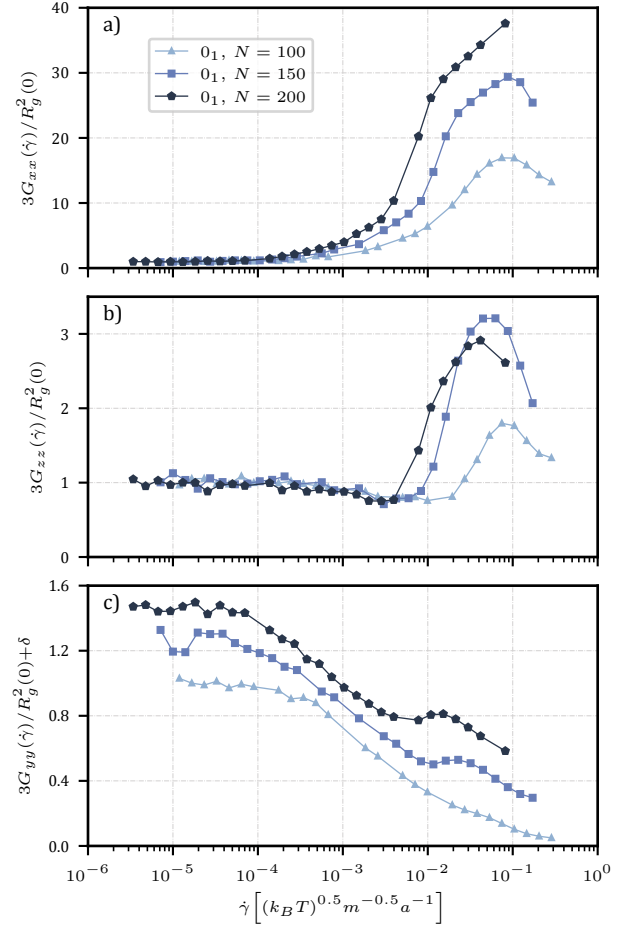


Figure 1. The gyration tensor diagonal elements $G_{\alpha\alpha}(\dot{\gamma})$, normalized over their equilibrium value $R_g^2(0)/3$, against the shear rate $\dot{\gamma}$. (a): G_{xx} (flow direction) increases with shear rate to some maximum and then drops as rings align into flow-vorticity plane and experience less strain. (b): G_{zz} (vorticity direction) decreases to a minimum and then shoots up at values of $\dot{\gamma}$ that anticipate the inflation anomaly observed in panel (c) for the gradient direction. (c): G_{yy} (gradient direction) initially decreases with shear rate. For $N = 150$ and $N = 200$, an inflation anomaly is observed, which is hardly visible for $N = 100$. To highlight this behavior, shifts δ have been applied along the vertical axis, where $\delta_{N=100} = 0.0$, $\delta_{N=150} = 0.25$ and $\delta_{N=200} = 0.5$.

unfolding of the polymer and a uniform expansion in all directions whilst the ring orientation in space remains fixed (see below) we term it *inflation phase*, induced by shear and hydrodynamics. After the development of the inflation phase, the ring becomes fully inflated or stretched.

Very recently, Young *et al.*^[27] applied Brownian Dynamics simulations of chains and rings in *mixed planar* flows, approximating the effects of hydrodynamics via the Rotne-Prager-Yamakawa (RPY) mobility tensor. Though

they did find a stretched phase for truly mixed flows that combine shear with extension, the inflation phase and the stretched configurations are absent in their findings for pure shear, corresponding to the value $\alpha = 0$ of the velocity gradient tensor $\bar{\Gamma}$ in the standard terminology of mixed flows^[27,74,75]. The absence of this phase in the aforementioned work could be a consequence of approximating hydrodynamics via the RPY-tensor but it is most likely an effect of the low degree of polymerization, $N = 120$, employed by Young *et al.* Further differences with Ref.^[27] pertain to the solvent quality (θ -solvent in Ref.^[27] vs. good quality solvent here) and to the modelling of the bonding interactions between the monomers (harmonic vs. FENE-springs, respectively). These details should not play an important role at sufficiently high Weissenberg numbers, however.

The shape parameters^[45,66,93,94] are following the same anomalous behavior. Two of them, the asphericity and the acylindricity are shown as representatives in Figs. 2a and 2b. Indeed, the non-monotonic behavior of the elements of the gyration tensor is directly reflected in similar non-monotonic trends as the aforementioned quantities. Very informative is the behavior of the orientational resistance $m_G = Wi \tan(2\theta)$ and of the alignment angle θ of the polymer with the flow axis, shown in Figs. 2c and 2d, offering a direct quantitative measure of the onset and the characteristics of the inflation phase. It can be seen that m_G shows a crossover from the usual, $m_G \sim \dot{\gamma}^{0.6}$ -behavior to a much sharper, $m_G \sim \dot{\gamma}$ power-law, which allows us to define a characteristic crossover shear rate $\dot{\gamma}_\times$ marked by the vertical lines in Fig. 2c and summarized in Table 2. The second regime immediately implies that the orientation angle θ does not change with the shear rate $\dot{\gamma}$, see also the Discussion Section below. Moreover, as a direct comparison between Figs. 1c, 2c and 2d shows, the regime between the local minimum and the local maximum of $G_{yy}(\dot{\gamma})$ coincides with the regime of the $m_G \sim \dot{\gamma}$ -scaling in which the orientation angle θ remains constant and the ring thus merely unfolds, growing in all directions – precisely the inflation phase mentioned above. Figs. 2e and 2f show that the same scenario also holds for some selected knotted topologies, to which we will return in the next subsection.

To further describe, analyze and understand shear-induced ring polymer inflation, we take a closer look at the $N = 200$ ring as an example:

- **In the tumbling regime:** At $\dot{\gamma} \cong 2.5 \times 10^{-3}$, G_{yy} first reaches the value of the anomaly maximum. We observe the formation of a tilting axis along which the polymer stretches. Tumbling frequently occurs and takes up substantial space in gradient direction. At $\dot{\gamma} \cong 3 \times 10^{-3}$, tumbling becomes less gradient-intense and occurs less frequently, but the tilting becomes more pronounced as fluctuations around the axis decrease.
- **During the inflation phase:** Before the anomaly maximum of G_{yy} , at $\dot{\gamma} \cong 8 \times 10^{-3}$, there are rare tumbling events as the ring starts to stabilize and open.

Ring topology	N	$\dot{\gamma}_\times [(k_B T)^{0.5} m^{-0.5} a^{-1}]$
0 ₁	100	9.8×10^{-3}
0 ₁	150	8.0×10^{-3}
0 ₁	200	5.9×10^{-3}
3 ₁	100	1.3×10^{-2}
3 ₁	200	5.1×10^{-3}
4 ₁	200	4.0×10^{-3}
5 ₁	200	4.7×10^{-3}
5 ₂	200	6.2×10^{-3}
6 ₁	200	6.6×10^{-3}
6 ₂	200	7.2×10^{-3}
6 ₃	200	6.4×10^{-3}
7 ₁	200	7.7×10^{-3}
8 ₁	200	7.9×10^{-3}

Table 2. Crossover Shear Rates. The crossover values $\dot{\gamma}_\times$ for the transition from the tumbling to the inflation phase of ring polymers with topology denoted at the left column and degree of polymerization N in the middle one. Note that for the cases of $N = 100$ (0₁ and 3₁-rings), a fully developed inflation phase does not emerge and $\dot{\gamma}_\times$ denotes there the crossover value between the two power-law regimes in Fig. 2(b).

Less fluctuations are visible.

- **In the fully inflated regime:** At $\dot{\gamma} \cong 1.5 \times 10^{-2}$, the anomaly reaches its peak. The polymer is aligned with the tilting axis and quite stable. Tumbling is extremely rare. Finally, at $\dot{\gamma} \cong 2 \times 10^{-2}$, the polymer does not tumble but looks almost rigid, while the tilting axis gets progressively closer to the flow axis.

During the inflation phase and all the way into the fully inflated configuration, a particular kind of tank-treading (TT) motion shows up in lieu of the suppressed tumbling. Contrary to the usual shear-induced TT in which the rotation axis lies parallel to the vorticity direction, here we have fluctuation-induced rigid rotations of the inflated molecule around an axis lying in the flow-gradient direction perpendicular to its tilt, i.e., almost parallel to the gradient direction since θ is small.

To visualize the contribution of the solvent, in conjunction with the closed polymer topology, to this behavior, we first compare the flow profiles established in the flow-vorticity plane around the polymer’s center-of-mass for contour lengths $N = 100$ and $N = 200$ as shown in Fig. 3. Qualitatively, the established flow fields are similar, but at the same shear rates, the $N = 200$ ring experiences a stronger backflow, and the shape and position of the horseshoe is more visible in the flow profile. At the maximum of the anomaly on G_{yy} at around $\dot{\gamma} = 0.02$ (Fig. 1c), Fig. 3d shows a clearly established backflow profile, while the same cannot be said about the $N = 100$ ring at the same shear rate (Fig. 3a).

The transition to the inflated phase is closely related to the pattern of inter-monomer and hydrodynamic forces acting on the ring. Due to the development of a strongly stretched configuration, the former are exclusively elastic forces from the tethering (FENE) potentials between suc-

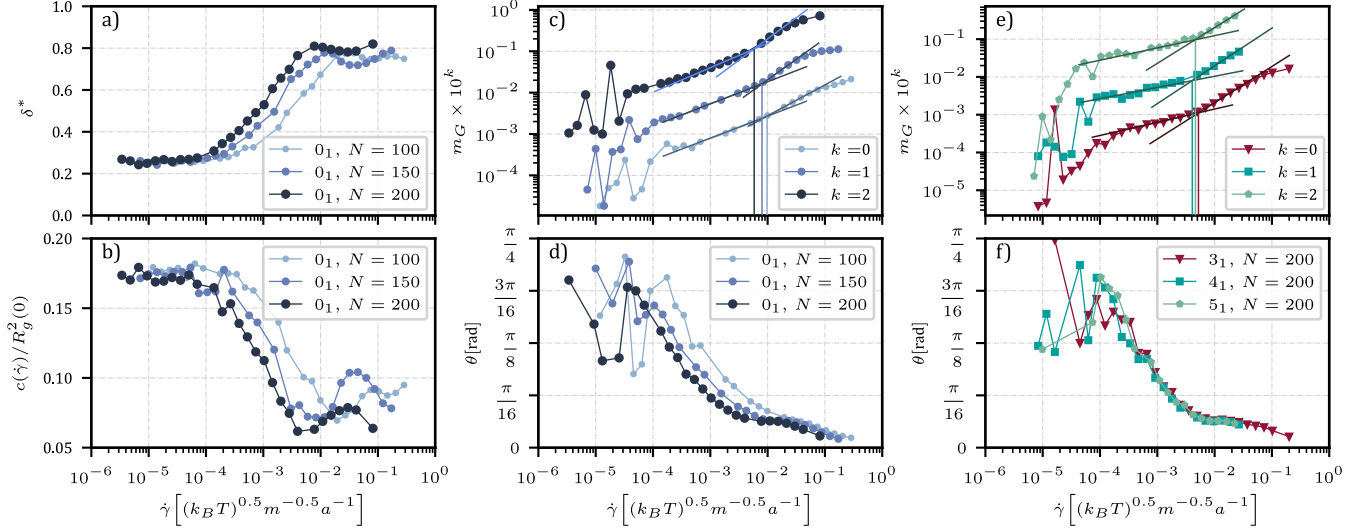


Figure 2. Shape and orientation of knotted and unknotted ring polymers under increasing shear rate $\dot{\gamma}$. (a): Anisotropy δ^* . (b): Acylindricity $c(\dot{\gamma})$ scaled over the squared gyration radius at $\dot{\gamma} = 0$. (c): Orientational resistance m_G for three different 0_1 -rings, as denoted in the label of panel (d). The vertical lines denote crossovers from the tumbling regime at the lower values of $\dot{\gamma}$ to the inflation regime at higher ones. The straight lines on the left of the crossover have slope 0.6 and the ones on the right have slope 0.85 for $N = 100$ and unity for $N = 150$ and $N = 200$. Curves have been multiplied by constants, providing vertical shifts as indicated in the label. (d): Alignment angle θ between the eigenvector corresponding to the largest eigenvalue of the gyration tensor and the flow axis for the three 0_1 -rings. (e): Orientational resistance for three different knotted rings of topologies as denoted in the label of panel (f). The straight lines on the left of the crossover points have slope 0.6 and the ones on the right have slope unity. The curves have been multiplied by constants, whose values are given in the label, for visual clarity. (f): Same as panel (d) but for the three knotted rings whose characteristics are summarized in the label.

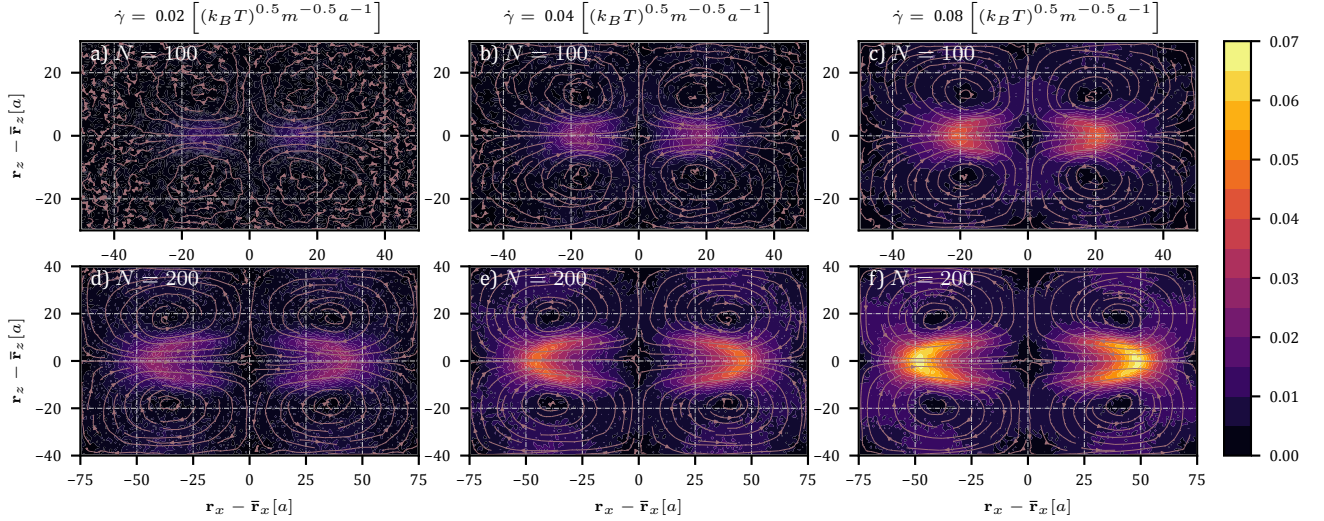


Figure 3. Flow fields in flow-vorticity plane centered around center of mass $\bar{\mathbf{F}}$ of an 0_1 ring. The colour map encodes velocity magnitudes in units of $[\sqrt{k_B T/m}]$. Left to right: Increasing shear rates $\dot{\gamma} = 0.02, 0.04, 0.08$ $[(k_B T)^{0.5} m^{-0.5} a^{-1}]$. Top to bottom: Increasing contour length $N = 100, 200$. Direct comparison between equal shear rates shows backflow is significantly more pronounced at $N = 200$.

cessive beads; contacts between monomers are extremely rare and excluded volume interactions are inactive there. In Figs. 6(a-c) we show the gradient-direction component of the inter-monomer force, $\bar{\mathbf{F}}_y$, as a function of the distance from the center of mass, for three different ring sizes and shear rates slightly below, slightly above and well above the crossover value $\dot{\gamma}_\times$ for each length. The observed force is always directed towards the center-of-mass and is strongest

near the latter, where also the tension along the chain is strongest, as can be seen in Fig. 6d. The gradient-component forces feature, for the two longest rings that undergo an inflation phase, a striking development as $\dot{\gamma}_\times$ is crossed: a prolonged region along the ring where $\bar{\mathbf{F}}_y \cong 0$ develops, which arises from the emergence of portions of the ring that remain essentially horizontal, so that no y -component of the force results, see Fig. 5b. At the same

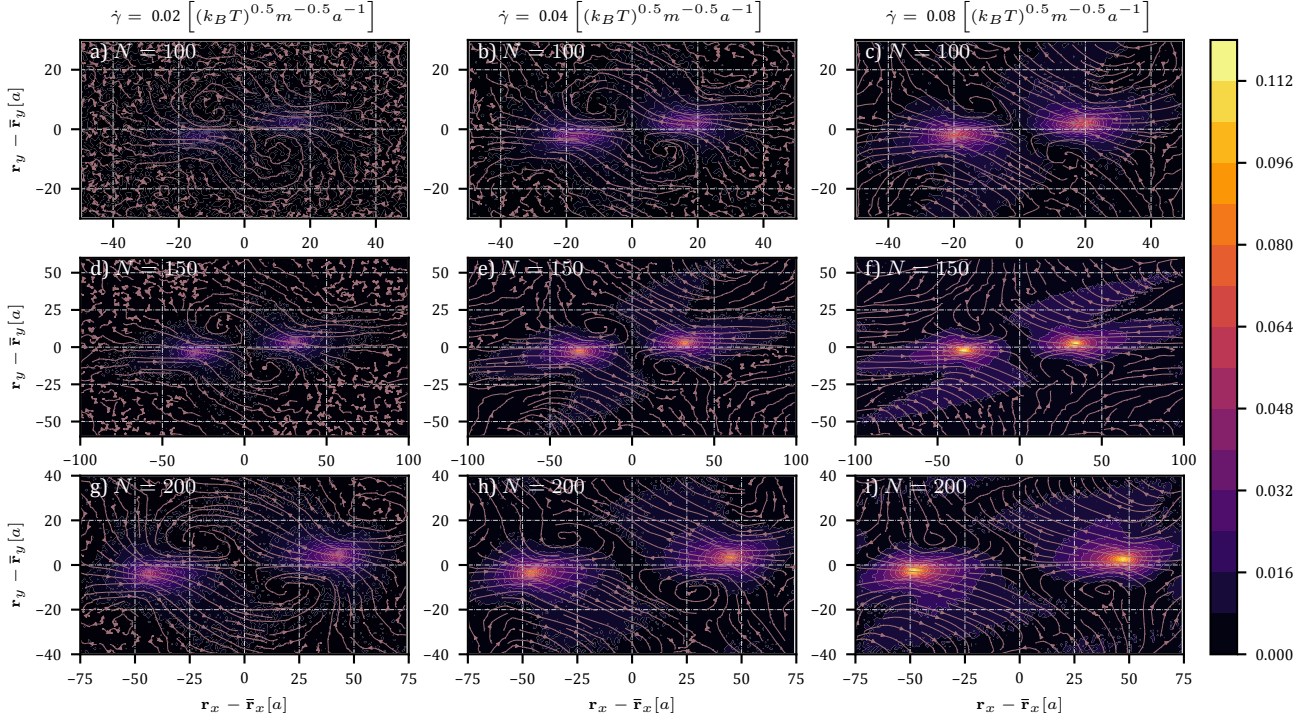


Figure 4. Flow fields in flow-gradient plane centered around center of mass $\bar{\mathbf{r}}$ of an 0_1 ring. The colour map encodes modified velocity magnitudes $\|\mathbf{v}'\|$ in units of $[\sqrt{k_B T/m}]$, $\mathbf{v}' = \mathbf{v} - \dot{\gamma}y\hat{\mathbf{x}}$. Left to right: Increasing shear rates $\dot{\gamma} = [0.02, 0.04, 0.08] [(k_B T)^{0.5} m^{-0.5} a^{-1}]$. Top to bottom: Increasing contour length $N = [100, 150, 200]$.

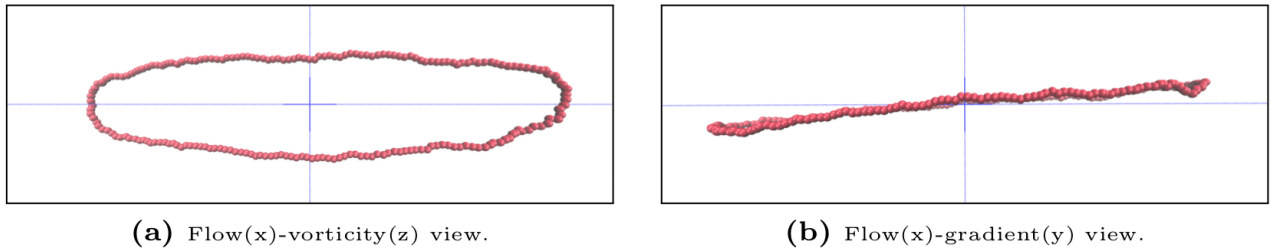


Figure 5. Typical and stable swollen configuration of the $N = 200$ 0_1 -ring, at $Wi = 543.95$ or $\dot{\gamma} = 2.1 \times 10^{-2} [(k_B T)^{0.5} m^{-0.5} a^{-1}]$. We have marked the flow (x) and vorticity (z) or gradient (y) axis in blue. The intersection is the polymer's center of mass. The solid part on each axis extends a length of $5[a]$ in either direction.

time, the fluid streams also smoothly and almost horizontally along these portions, see Figs. 4e and 4h, so that the ring is at stable equilibrium there. At the tips of the ring, as well as close to their centers, the inter-monomer forces tend to push the beads towards the neutral plane and they are counteracted by hydrodynamic forces of the streaming solvent, which is deflected on the polymer, see Fig. 4. As we move to higher shear rates, this region gets smaller, and there are stronger forces acting on beads far away from the center-of-mass.

Referring to the typical shear rates $\dot{\gamma}_1$, $\dot{\gamma}_2$, and $\dot{\gamma}_3$ in Figs. 6(a-c), we propose the following response patterns to shear for rings of sufficiently large contour length. As shear rate increases from equilibrium, ring polymers start swelling first in flow direction and align with an axis in the flow-gradient plane. They fluctuate around this axis, and occasionally experience tumbling because of sufficiently strong fluctuations of the horseshoe regions. Approaching $\dot{\gamma}_1$, tumbling becomes enhanced and the knot starts to experience backflow from the horseshoe regions. Near $\dot{\gamma}_2$, tumbling stops completely. The backflow causes so much tension along the ring that fluctuations are suppressed. For tumbling to occur, an entire section of the ring would have to angle towards the center-of-mass plane. At the same time, during the transition between $\dot{\gamma}_1$ and $\dot{\gamma}_2$, the alignment angle is almost constant, so the extension of the ring in gradient direction, and by extension the strength of shear and backflow, scales proportional to shear rate. Eventually, transitioning from $\dot{\gamma}_2$ to $\dot{\gamma}_3$, the sheared solvent flows powerfully enough to push the ring into the flow-vorticity plane, and the hydrostatic bubble becomes less and less pronounced. In contrast, rings with low contour length never experience a point where fluctuations are suppressed enough to prevent tumbling, and a local maximum for G_{yy} does not show up.

Collapse of all knots and localization in space. We have also investigated and compared behavior of knotted rings and report very similar behavior under strong shear. The diagonal entries of the gyration tensor (Fig. 7a-c) all show the same qualitative behavior, and across all knot topologies, and the anomaly is present for G_{yy} (Fig. 7c). The stabilization of the alignment angle is common across all topological varieties as well (Fig. 7d), and we conclude that shape-wise, it is justified to talk about a generic behavior of ring-shaped topologies rather than just of the 0_1 ring.

All knotted sections are pulled tight (Fig. 7f) and stay small for the remainder of the simulation, essentially filling the role of a particularly bulky bead. This bead-like knotted section has a preferred position on the ring, although this constraint might be lifted as the ring aligns more and more with the flow axis. Below this threshold, however, the knot tends to be located on the horseshoe-region of the ring (Fig. 7e) and, as tumbling is suppressed, only has tank-treading as a possible way to move swiftly. In this sense, the knotted section acts as a stabilization anchor for the ring, which already experiences a strongly suppressed,

fluctuating form of tank-treading rather than a pronounced one^[26]. The knotted section adds to this effect. When the knotted section does move, and when it manages to leave the horseshoe region, it very quickly tank-treads to the opposite horseshoe region to stabilize there again.

Discussion

Interpretation of results. To understand the physical mechanism behind the transition from the tumbling to the inflation phase and to make quantitative predictions about its occurrence, we need to properly understand the interplay between polymer orientation in the shear field and the hydrodynamic forces imposed on it by the solvent. In Fig. 8(a) the average tilt angle θ of the ring is shown, subtended by the vector corresponding to the largest eigenvalue of the gyration tensor and the flow axis, alongside with the elevation y_e of the tip at the horseshoe region of the ring. In Fig. 8(b) a top view of the ring is shown, featuring an open ellipsoidal shape characteristic of the swelling in the vorticity direction, caused by the backflow of the solvent reflected in the horseshoe regions^[26]. Due to the form of the flow pattern, shown in Fig. 3 and sketched in Fig. 8(b) by the curved green arrows, the whole ring experiences an outwards pointing inflation force (akin to the pressure in the interior of an elastic bubble) and thus it can be thought of as a succession of tension blobs. The largest of these, having size ξ_T , is located at the tips of the ring. A necessary condition for tumbling is

$$\xi_T \geq y_e, \quad (2)$$

so that parts of the upper (lower) tip of the ring can be found below (above) the neutral plane and carried to the opposite direction by the streaming fluid. Accordingly, we need to estimate the dependence of y_e and ξ_T on the shear rate $\dot{\gamma}$.

From geometrical considerations, we have

$$y_e \cong \sqrt{G_{xx}} \tan \theta \cong \sqrt{G_{xx}} \theta, \quad (3)$$

for small values of θ , typical of the transition to the inflation phase. The flow-direction component of the gyration tensor, G_{xx} scales in the tumbling regime as $G_{xx}(\dot{\gamma})/G_{xx}(0) \sim Wi^{0.6}$ ^[26,95]. Keeping in mind that $G_{xx}(0) \propto R_g^2(0) \sim N^{2\nu}$ with the Flory exponent $\nu \cong 0.588$, the above considerations yield

$$\sqrt{G_{xx}} \sim \dot{\gamma}^{0.3} \tau_R^{0.3} N^\nu. \quad (4)$$

The dependence of the tilt angle θ on the shear rate can be extracted from the scaling of the orientational resistance $m_G = Wi \tan(2\theta) \cong 2\theta Wi$ on the Weissenberg number: $m_G \sim Wi^{0.6}$, implying

$$\theta \sim \dot{\gamma}^{-0.4} \tau_R^{-0.4}. \quad (5)$$

Combining Eqs. (3), (4) and (5) above, together with the power-law $\tau_R \sim N^{3\nu}$ for the dependence of the longest relaxation time of the polymer on N , we obtain

$$y_e \sim \dot{\gamma}^{-0.1} N^{0.4}, \quad (6)$$

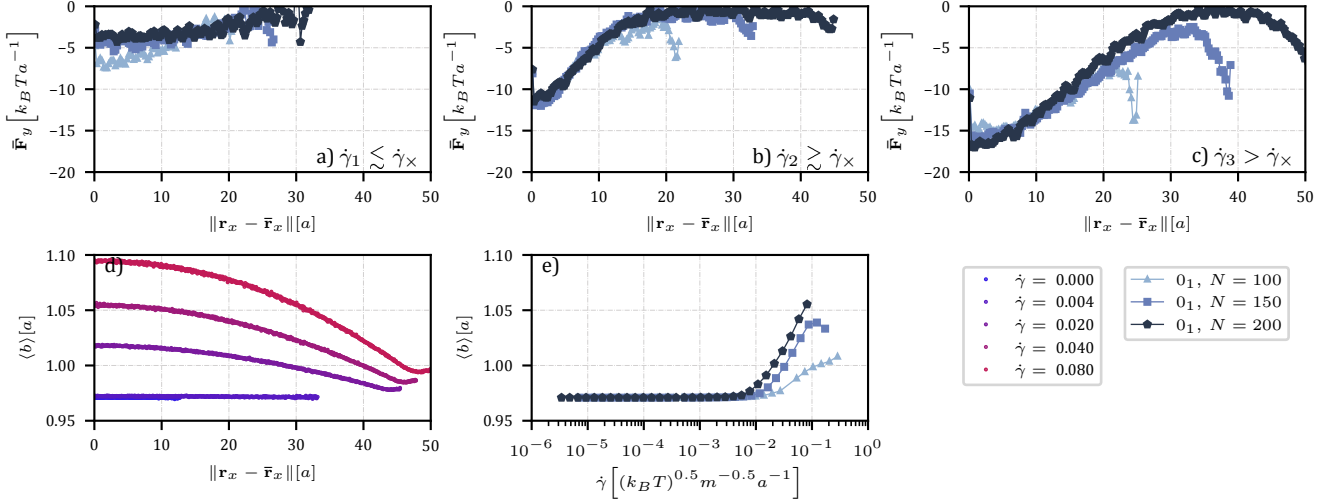


Figure 6. Inter-monomer forces (a-c) and bond extension along the ring (d-e). (a-c): Gradient-direction component of force on beads, averaged in intervals along flow axis and measured relative to center-of-mass. A negative sign signifies pull towards center-of-mass. Shear rate increasing from (a) to (c). (a): At $\dot{\gamma}_1 = [0.020, 0.006, 0.003]$ for $N = [100, 150, 200]$, G_{yy} first takes on the value of its local maximum. This has to be estimated for $N = 100$, where monotony is maintained. (b): At $\dot{\gamma}_2 = [0.040, 0.020, 0.018]$ for $N = [100, 150, 200]$, G_{yy} reaches its local maximum. (c): At $\dot{\gamma}_3 = [0.286, 0.171, 0.082]$ for $N = [100, 150, 200]$, G_{yy} has gotten substantially smaller than it was at the local maximum. (d): Bond extension of the $N = 200$ ring along flow axis. $0.97 [a]$ is the average for equilibrium with the parameters given in the simulation. (e): Average bond extension increasing with shear rate.

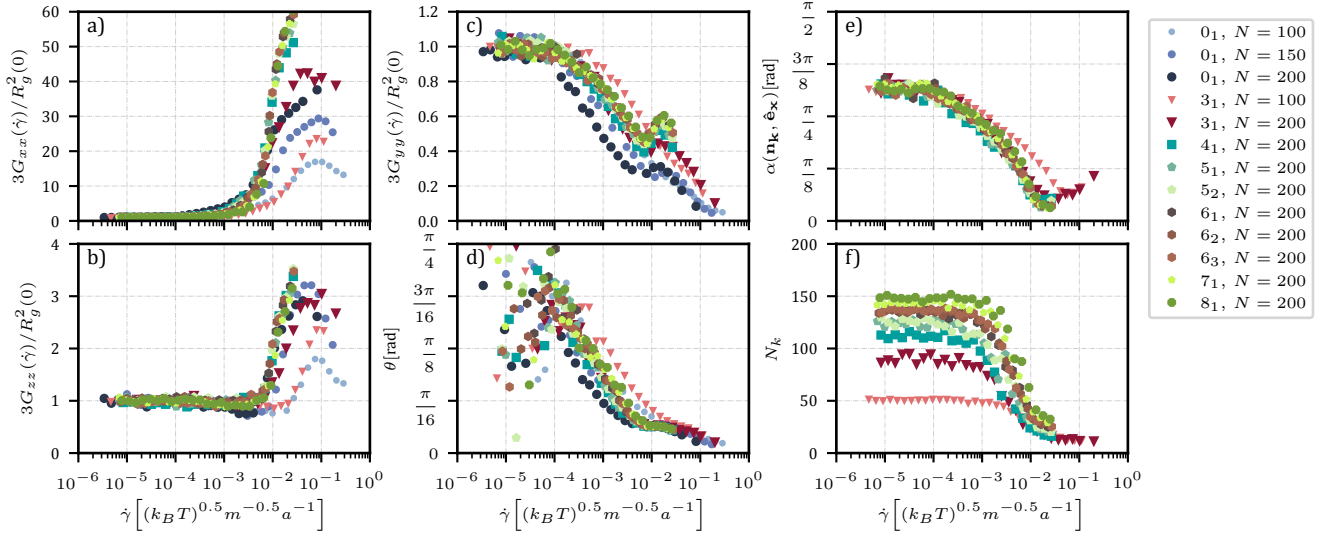


Figure 7. Shape and orientation of knotted ring topologies under increasing shear rate $\dot{\gamma}$. (a): G_{xx} (flow), (b): G_{zz} (vorticity), (c): G_{yy} (gradient), (d): alignment angle θ , (e): angle α between vector \mathbf{n}_k from the ring's to the knotted section's center of mass and axis vector $\hat{\mathbf{x}}$, and (f): number of beads on the knotted section, N_k . Under strong shear, all knot topologies behave almost exactly like a ring with the same contour length N . Different colors correspond to different knot types, as indicated in the legend.

where the approximation $0.7\nu \cong 0.4$ has been employed.

The magnitude of the inflating force F that stretches the ring and gives rise to the tension blobs is set by the streaming velocity of the solvent at the point of highest elevation y_e and it scales as $F \sim \dot{\gamma} y_e$. The ensuing tension blob size scales as $\xi_T \sim k_B T / F \sim \dot{\gamma}^{-1} y_e^{-1}$, resulting, together with Eq. (6) above, into

$$\xi_T \sim \dot{\gamma}^{-0.9} N^{-0.4}. \quad (7)$$

Evidently, ξ_T decreases with the shear rate $\dot{\gamma}$ much faster than y_e , so that beyond a crossover shear rate $\dot{\gamma}_x$, the inequality (2) cannot be fulfilled and tumbling stops, the ring transitioning into the inflation phase. Putting together Eqs. (2), (6), and (7), we find the dependence of $\dot{\gamma}_x$ with N to follow a simple power-law:

$$\dot{\gamma}_x \sim \frac{k_B T}{\eta \sigma^3} N^{-1}, \quad (8)$$

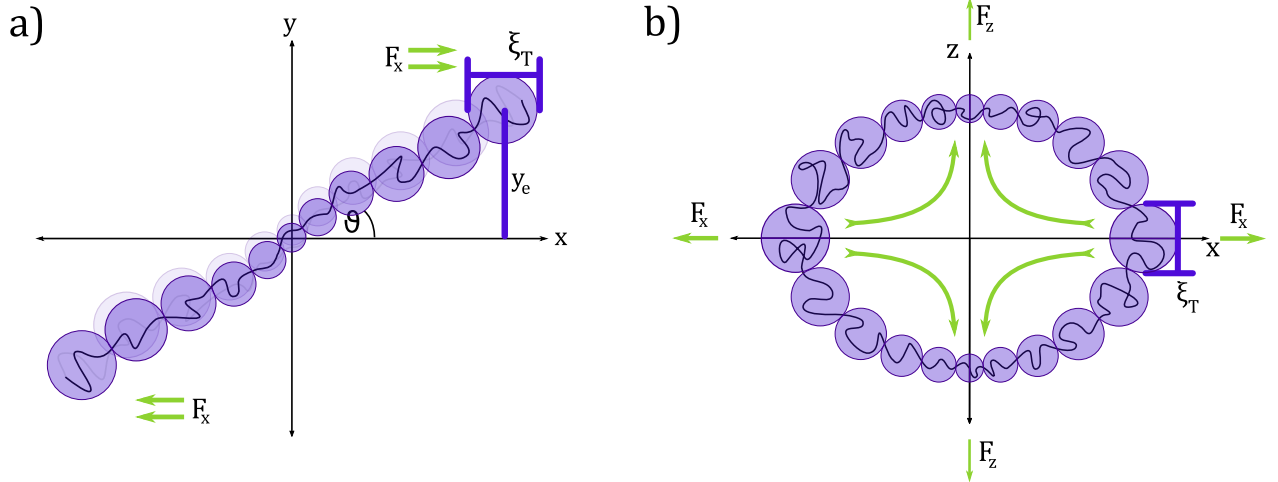


Figure 8. Sketch of a ring polymer under steady shear. (a): Viewed projected on the flow-gradient (x - y) plane, the ring is rendered as a succession of blobs, the largest of which is located at the tips and has size ξ_T . The elevation of the tip over the neutral (flow-vorticity) plane is y_e and the tilt angle is θ . (b): Viewed projected onto the flow-vorticity (x - z) plane, the ring has an oval shape and it is stretched outwards in all directions due to backflow of solvent (denoted by the curved green arrows), reflected at the two horseshoe-shaped regions at the tips.

where we have reintroduced in the prefactor the quantities entering in the expressions of y_e and F , to obtain the full dependence on the temperature, solvent viscosity and monomer size as well.

There is a striking comparison that can be made here with the case of suspensions of colloidal particles of size d under shear. There, the Peclet number Pe , which scales as

$$Pe \sim \frac{\eta \dot{\gamma} d^3}{k_B T}, \quad (9)$$

expresses the typical ratio of timescales for Brownian and shear-induced motions^[96]. The Brownian character of the motion dominates for $Pe \lesssim 1$ whereas shear takes over for $Pe > 1$ and the particles become fully non-Brownian for $Pe \gg 1$. Accordingly, and defining a crossover value $Pe_\times = 1$ between the two regimes, this translates, for colloidal particles, into a crossover shear rate

$$\dot{\gamma}_\times \sim \frac{k_B T}{\eta d^3}. \quad (10)$$

Comparing Eqs. (8) and (10), we see that the former is fully consistent with the interpretation and the physical picture of the inflated, stressed ring as a succession of N particles of size σ held together by essentially rigid connections. The fact that it has been derived independently, using scaling arguments from polymer theory, and at the same time it turns out to deliver a physically consistent picture of an inflated polymer as a rigid, non-Brownian colloid, offers additional corroboration of its validity.

Using the typical orders of magnitude, $\eta \cong 10$ and $N \cong 10^2$ employed in this work, we obtain $\dot{\gamma}_\times \cong 10^{-3}$, in satisfactory agreement with the results in Table 2. Though we have only simulated rings with three different N -values, the results shown in Fig. 2(b) and summarized in Table

2 also support the above power-law prediction. Moreover, translating the crossover shear rate into a crossover Weissenberg number $Wi_\times = \dot{\gamma}_\times \tau_R$ and using the scaling $\tau_R \sim N^{3\nu}$, we obtain $Wi_\times \sim N^{0.76}$. Accordingly, employing ring polymers of high N guarantees that the condition of lying in the strongly nonlinear regime, $Wi_\times \gg 1$, is satisfied. At the same time, increasing N lowers the value $\dot{\gamma}_\times$ of the shear rate at which the transition to the inflation phase will take place, therefore making the phenomenon more easily observable experimentally.

Once the rings enter their inflation phase, the orientational resistance scales as $m_G \sim Wi$, directly implying $\theta \sim Wi^0$: the orientation angle remains constant during this phase and the ring simply fully unfolds until the tension blob reaches the monomer size. Thereafter, it behaves as a rigid, non-Brownian object for which thermal fluctuations play no role. The highest elevation scales as $y_e \sim N$ [cf. Eq. (6)] and the hydrodynamic force on the monomers scales, accordingly, as $F \sim \dot{\gamma} N$, cf. $F \sim \dot{\gamma}^{0.9} N^{0.4}$ in the tumbling regime.

Filter for chains and rings. The swelling of rings in vorticity direction is exclusive to their closed structure and their transition to the stretched, inflated configuration is size-specific. Accordingly, we surmise that this property could be employed in a simple microfluidic device to enhance separation of large and small rings in a mixture under Poiseuille flow. Indeed, the latter creates a parabolic velocity profile for the Newtonian solvent in which the mixture is suspended, causing thereby a position-varying shear rate $\dot{\gamma}(y)$ across the gradient direction y . This local shear rate has a maximum close to the walls and vanishes in the middle of the channel. Large rings exposed to high shear close to the walls will inflate and stretch, orient themselves al-

most parallel to the wall and thus be subject to both steric constraints with one another and strong lift forces from the wall. It is thus natural to expect that they will migrate towards the center of the channel, and displacing from there smaller rings that will be pushed towards the walls. In this way, a flow-induced size separation via focusing of the large rings in the middle can be achieved. The same is expected to be true for linear-ring mixtures.

Conclusion

We have shown that ring polymers in the presence of fully-developed hydrodynamic interactions behave remarkably different from chains, stars, branched or cross-linked polymers under pure, steady shear alone. They show a unique inflation in the vorticity direction because of a well-established backflow, which highlights the importance of carefully realized hydrodynamics when dealing with such closed topologies. For rings with high contour length, an interplay between alignment at an angle to the flow axis and the backflow causes the ring to self-stabilize in gradient direction and leads to a surcease of tumbling and a suppression of tank-treading. The entire object looks and behaves more like a rigid ring in this configuration and it behaves in this way even in the presence of complex knots along its backbone. On the basis of these phenomena, we suggest a potential microfluidic filter to separate rings from chains, or rings of different sizes from each other. As a knotted section on a sufficiently long ring has very sharp tank-treading-like transitions from one side of an open ring to another, we also envision that fluorescence techniques could be used to detect the presence of such a tight knot on a ring.

Although the present work was focused on single-molecule numerical experiments, future extensions should focus on the effects of shear and of the ring-stretching transition to the rheological behavior of dilute or semidilute ring polymer mixtures, as well as on the interplay between inflation and polymer rigidity. The former should be directly comparable with rheology experiments on ring polymer solutions, whereas the latter system can be realized by employing, e.g., short DNA rings. Work along these lines is currently under way.

Acknowledgments

The authors thank Luca Tubiana for supplying them with his LocKnot program for knot localization, and Dimitris Vlassopoulos for a critical reading of the manuscript and helpful discussions. The computational results presented have been achieved in part using the Vienna Scientific Cluster (VSC). M.L. has been supported in part by the uni:docs Doctoral Fellowship Programme of the University of Vienna.

References

- [1] A Grosberg and S Nechaev. Polymer Topology. *Adv. Pol. Sci.*, 106:1–29, 1993.
- [2] M. D. Frank-Kamenetskii, A. V. Lukashin, and A. V. Volodskii. Statistical mechanics and topology of polymer chains. *Nature*, 258:398–402, 1975.
- [3] V. Katritch, J. Bednar, D. Michoud, R. G. Scharein, J. Dubochet, and A. Stasiak. Geometry and physics of knots. *Nature*, 384:142–145, 1996.
- [4] C. Micheletti, D. Marenduzzo, and E. Orlandini. Polymers with spatial or topological constraints: Theoretical and computational results. *Phys. Rep.*, 504:1–73, 2011.
- [5] M. Kapnistos, M. Lang, D. Vlassopoulos, W. Pyckhout-Hintzen, D. Richter, D. Cho, T. Chang, and M. Rubinstein. Unexpected power-law stress relaxation of entangled ring polymers. *Nature Materials*, 7:997–1002, 2008.
- [6] Q. Huang, J. Ahn, D. Parisi, T. Chang, O. Hassager, S. Panyukov, M. Rubinstein, and D. Vlassopoulos. Unexpected Stretching of Entangled Ring Macromolecules. *Phys. Rev. Lett.*, 122(20):208001, MAY 22 2019.
- [7] N. T. Moore, R. C. Lua, and A. Yu. Grosberg. Topologically driven swelling of a polymer loop. *PNAS*, 101:13431–13435, 2004.
- [8] N. T. Moore and A. Yu. Grosberg. Limits of analogy between self-avoidance and topology-driven swelling of polymer loops. *Phys. Rev. E*, 72:061803, 2005.
- [9] M. Bohn and D. W. Heermann. Topological Interactions between ring polymers: Implications for chromatin loops. *J. Chem. Phys.*, 132:044904, 2010.
- [10] A. Narros, A. J. Moreno, and C. N. Likos. Influence of topology on effective potentials: coarse-graining ring polymers. *Soft Matter*, 6:2435–2441, 2010.
- [11] Thomas Vettorel, Alexander Y. Grosberg, and Kurt Kremer. Statistics of polymer rings in the melt: a numerical simulation study. *Phys. Biol.*, 6(2):025013, JUN 2009.
- [12] Jonathan D. Halverson, Won Bo Lee, Gary S. Grest, Alexander Y. Grosberg, and Kurt Kremer. Molecular dynamics simulation study of nonconcatenated ring polymers in a melt. I. Statics. *J. Chem. Phys.*, 134(20):204904, MAY 28 2011.
- [13] T. Sakaue. Ring Polymers in Melts and Solutions: Scaling and Crossover. *Phys. Rev. Lett.*, 106:167802, 2011.
- [14] Alexander Y. Grosberg. Annealed lattice animal model and Flory theory for the melt of non-concatenated rings: towards the physics of crumpling. *Soft Matter*, 10(4):560–565, 2014.
- [15] Jonathan D. Halverson, Jan Smrek, Kurt Kremer, and Alexander Y. Grosberg. From a melt of rings to chromosome territories: the role of topological constraints in genome folding. *Rep. Progr. Phys.*, 77(2):022601, FEB 2014.
- [16] Jan Smrek and Alexander Y. Grosberg. Understanding the dynamics of rings in the melt in terms of the annealed tree model. *J. Phys.: Condensed Matter*, 27(6):064117, FEB 18 2015.
- [17] Jan Smrek and Alexander Y. Grosberg. Minimal Surfaces on Unconcatenated Polymer Rings in Melt. *ACS Macro Lett.*, 5(6):750–754, JUN 2016.
- [18] Jonathan D. Halverson, Gary S. Grest, Alexander Y. Grosberg, and Kurt Kremer. Rheology of Ring Polymer Melts: From Linear Contaminants to Ring-Linear Blends. *Phys. Rev. Lett.*, 108(3):038301, JAN 18 2012.
- [19] Rossana Pasquino, Thodoris C. Vasilakopoulos, Youn Cheol Jeong, Hyojoon Lee, Simon Rogers, George Sakellariou, Juergen Allgaier, Atsushi Takano, Ana R. Bras, Taihyun Chang, Sebastian Goossen, Wim Pyckhout-Hintzen, Andreas Wischniewski, Nikos Hadjichristidis, Dieter Richter, Michael Rubinstein, and Dimitris Vlassopoulos. Viscosity of Ring Polymer Melts. *ACS Macro Lett.*, 2(10):874–878, OCT 2013.
- [20] Sebastian Goossen, Ana R. Bras, Wim Pyckhout-Hintzen, Andreas Wischniewski, Dieter Richter, Michael Rubinstein, Jacques Roovers, Pierre J. Lutz, Youncheol Jeong, Taihyun Chang, and Dimitris Vlassopoulos. Influence of the Solvent Quality on Ring Polymer Dimensions. *Macromolecules*, 48(5):1598–1605, MAR 10 2015.
- [21] Davide Michieletto and Matthew S. Turner. A topologically driven glass in ring polymers. *Proc. Nat. Acad. Sci. U.S.A.*

- 113(19):5195–5200, MAY 10 2016.
- [22] Davide Michieletto, Davide Marenduzzo, Enzo Orlandini, and Matthew S. Turner. Ring Polymers: Threadings, Knot Electrophoresis and Topological Glasses. *Polymers*, 9(8):349, AUG 2017.
- [23] Davide Michieletto, Negar Nahali, and Angelo Rosa. Glassiness and Heterogeneous Dynamics in Dense Solutions of Ring Polymers. *Phys. Rev. Lett.*, 119(19):197801, NOV 7 2017.
- [24] Y. Li, K.-W. Hsiao, C. A. Brockman, D. Y. Yates, R. M. Robertson-Anderson, J. A. Kornfield, M. J. San Francisco, C. M. Schroeder, and G. B. McKenna. When ends meet: Circular DNA stretches differently in elongational flows. *Macromolecules*, 48:5997–6001, 2015.
- [25] K.-W. Hsiao, C. M. Schroeder, and C. E. Sing. Ring polymer dynamics are governed by a coupling between architecture and hydrodynamic interactions. *Macromolecules*, 49:1961–1971, 2016.
- [26] M. Liebetreu, M. Ripoll, and C. N. Likos. Trefoil Knot Hydrodynamic Delocalization on Sheared Ring Polymers. *ACS Macro Lett.*, 7:447–452, 2018.
- [27] Charles D. Young, June R. Qian, Michael Marvin, and Charles E. Sing. Ring polymer dynamics and tumbling-stretch transitions in planar mixed flows. *Phys. Rev. E*, 99:062502, 2019.
- [28] K. Koniaris and M. Muthukumar. Knottedness in ring polymers. *Phys. Rev. Lett.*, 66:2211–2214, 1991.
- [29] S. A. Wasserman and N. R. Cozzarelli. Biochemical topology: Applications to DNA recombination and replication. *Science*, 232:951–960, 1986.
- [30] V. V. Rybenkov, N. R. Cozzarelli, and A. V. Vologodskii. Probability of DNA knotting and the effective diameter of the DNA double helix. *Proc. Natl. Acad. Sci. USA*, 90:5307–5311, 1993.
- [31] C. Micheletti, D. Marenduzzo, E. Orlandini, and D. W. Sumners. Simulations of Knotting in Confined Circular DNA. *Biophysical Journal*, 95:3591–3599, 2008.
- [32] P. Virnau, L. A. Mirny, and M. Kardar. Intricate knots in proteins: Function and evolution. *PLoS Comput. Biol.*, 2:e122, 2006.
- [33] J. I. Sulkowska, J. K. Noel, and J. N. Onuchic. Energy landscape of knotted protein folding. *Proc. Natl. Acad. Sci. USA*, 109:17783–17788, 2012.
- [34] P. Dabrowski-Tumanski and J. I. Sulkowska. Topological knots and links in proteins. *Proc. Natl. Acad. Sci. USA*, 114:3415–3420, 2017.
- [35] Y. Arai, R. Yashuda, K. Akashi, Y. Harada, H. Miyata, K. Kinoshita Jr., and H. Itoh. Tying a molecular knot with optical tweezers. *Nature*, 399:446–448, 1999.
- [36] X. R. Bao, H. J. Lee, and S. R. Quake. Behavior of Complex Knots in Single DNA Molecules. *Phys. Rev. Lett.*, 91:265506, 2003.
- [37] D. Leigh, S. L. Woltering, and S. D. P. Fielden. Molecular knots. *Angew. Chem. Int. Ed.*, 56:11166–11194, 2017.
- [38] A. Yu. Grosberg, A. Feigel, and Y. Rabin. Flory-type theory of a knotted ring polymer. *Phys. Rev. E*, 54:6618–6622, 1996.
- [39] A. Yu. Grosberg. Critical Exponents for Random Knots. *Phys. Rev. Lett.*, 85:3858–3861, 2000.
- [40] V. Katritch, W. K. Olson, A. Vologodskii, J. Dubochet, and A. Stasiak. Tightness of random knotting. *Phys. Rev. E*, 61:5545–5549, 2000.
- [41] A. Y. Grosberg and Y. Rabin. Metastable tight knots in a wormlike polymer. *Phys. Rev. Lett.*, 99:217801, 2007.
- [42] M. L. Mansfield and J. F. Douglas. Properties of knotted ring polymers. I. Equilibrium dimensions. *J. Chem. Phys.*, 133:044903, 2010.
- [43] M. L. Mansfield and J. F. Douglas. Properties of knotted ring polymers. II. Transport properties. *J. Chem. Phys.*, 133:044904, 2010.
- [44] L. Tubiana, A. Rosa, F. Fragiaco, and C. Micheletti. Spontaneous knotting and unknotting of flexible linear polymers: Equilibrium and kinetic aspects. *Macromolecules*, 46(9):3669–3678, 2013.
- [45] A. Narros, A. J. Moreno, and C. N. Likos. Effects of Knots on Ring Polymers in Solvents of Varying Quality. *Macromolecules*, 46:3654–3668, 2013.
- [46] L. Dai and P. S. Doyle. Effects of intrachain interactions on the knot size of a polymer. *Macromolecules*, 49:7581–7587, 2016.
- [47] S. R. Quake. Topological effects of knots in polymers. *Phys. Rev. Lett.*, 73:3317–3320, 1994.
- [48] P.-Y. Lai. Dynamics of polymer knots at equilibrium. *Phys. Rev. E*, 66:021805, 2002.
- [49] Y.-J. Sheng and K.-L. Cheng. Polymer knot confined in a tube: Statics and relaxation dynamics. *Phys. Rev. E*, 65:011801, 2001.
- [50] C. Micheletti and E. Orlandini. Numerical study of linear and circular model DNA chains confined in a slit: metric and topological properties. *Macromolecules*, 45:2113–2121, 2012.
- [51] L. Dai, J. R. C. van der Maarel, and P. S. Doyle. Effect of nanoslit confinement on the knotting probability of circular DNA. *ACS Macro Lett.*, 1:732–736, 2012.
- [52] C. H. Nakajima and T. Sakaue. Localization and size distribution of a polymer knot confined in a channel. *Soft Matter*, 9:3140–3146, 2013.
- [53] G. D’Adamo and C. Micheletti. Molecular Crowding Increases Knots Abundance in Linear Polymers. *Macromolecules*, 48:6337–6346, 2015.
- [54] L. Dai, C. B. Renner, and P. S. Doyle. Metastable knots in confined semiflexible chains. *Macromolecules*, 48:2812–2818, 2015.
- [55] A. R. Klotz, V. Narsimhan, B. W. Soh, and P. S. Doyle. Dynamics of DNA knots during chain relaxation. *Macromolecules*, 50:4074–4082, 2017.
- [56] M. Marendza, E. Orlandini, and C. Micheletti. Sorting ring polymers by knot type with modulated nanochannels. *Soft Matter*, 13:795–802, 2017.
- [57] A. M. Saitta, P. D. Soper, E. Wasserman, and M. L. Klein. Influence of a knot on the strength of a polymer strand. *Nature*, 399:46–48, 1999.
- [58] Y.-J. Sheng, P.-Y. Lai, and H.-K. Tsao. Deformation of a stretched polymer knot. *Phys. Rev. E*, 61:2895–2901, 2000.
- [59] O. Farago, Y. Kantor, and M. Kardar. Pulling knotted polymers. *EPL*, 60:53–59, 2002.
- [60] Jing Tang, Ning Du, and Patrick S. Doyle. Compression and self-entanglement of single DNA molecules under uniform electric field. *Proc. Nat. Acad. Sci. U.S.A.*, 108(39):16153–16158, SEP 27 2011.
- [61] R. Matthews, A. A. Louis, and C. N. Likos. Effect of bending rigidity on the knotting of a polymer under tension. *ACS Macro Lett.*, 1:1352–1356, 2012.
- [62] P. Poier, C. N. Likos, and R. Matthews. Influence of Rigidity and Knot Complexity on the Knotting of Confined Polymers. *Macromolecules*, 47:3394–3400, 2014.
- [63] M. Caraglio, C. Micheletti, and E. Orlandini. Stretching response of knotted and unknotted polymer chains. *Phys. Rev. Lett.*, 115:188301, 2015.
- [64] Alexander R. Klotz, Beatrice W. Soh, and Patrick S. Doyle. Motion of Knots in DNA Stretched by Elongational Fields. *Phys. Rev. Lett.*, 120(18):188003, MAY 3 2018.
- [65] Magdalena Gruziel, Krishnan Thyagarajan, Giovanni Dietler, Andrzej Stasiak, Maria L. Ekiel-Jezewska, and Piotr Szymczak. Periodic motion of sedimenting flexible knots. *Phys. Rev. Lett.*, 121:127801, Sep 2018.
- [66] M. Ripoll, R. G. Winkler, and G. Gompper. Star Polymers in Shear Flow. *Phys. Rev. Lett.*, 96:188302, 2006.
- [67] M. Ripoll, R. G. Winkler, and G. Gompper. Hydrodynamic screening of star polymers in shear flow. *Eur. Phys. J. E*, 23:349–354, 2007.
- [68] C.-C. Huang, R. G. Winkler, G. Sutmann, and G. Gompper. Semidilute polymer solutions at equilibrium and under shear flow. *Macromolecules*, 43:10107–10116, 2010.
- [69] C. C. Huang, G. Sutmann, G. Gompper, and R. G. Winkler. Tumbling of polymers in semidilute solution under shear flow. *Europhys. Lett.*, 93:54004, 2011.
- [70] D. A. Fedosov, S. P. Singh, A. Chatterji, R. G. Winkler, and G. Gompper. Semidilute solutions of ultra-soft colloids under shear flow. *Soft Matter*, 8:4109–4120, 2012.
- [71] A. Nikoubashman and C. N. Likos. Branched Polymers under

- Shear. *Macromolecules*, 43:1610–1620, 2010.
- [72] Diego Jaramillo-Cano, Maud Formanek, Christos N. Likos, and Manuel Camargo. Star Block-Copolymers in Shear Flow. *J. Phys. Chem. B*, 122:4149–4158, 2018.
- [73] Maud Formanek and Angel J. Moreno. Single-Chain Nanoparticles under Homogeneous Shear Flow. *Macromolecules*, 52(4):1821–1831, FEB 26 2019.
- [74] Joe S. Hur, Eric S. G. Shaqfeh, Hazen P. Babcock, and Steven Chu. Dynamics and configurational fluctuations of single DNA molecules in linea mixed flows. *Phys. Rev. E*, 66:011915, 2002.
- [75] N. J. Woo and E. S. G. Shaqfeh. The configurational phase transitions of flexible polymers in planar mixed flows near simple shear. *J. Chem. Phys.*, 119:2908–2914, 2003.
- [76] P. S. Lang, B. Obermayer, and E. Frey. Dynamics of a semiflexible polymer or polymer ring in shear flow. *Phys. Rev. E*, 89:022606, 2014.
- [77] A. Malevanets and R. Kapral. Mesoscopic model for solvent dynamics. *J. Chem. Phys.*, 110(17):8605–8613, 1999.
- [78] A. W. Lees and S. F. Edwards. The computer study of transport processes under extreme conditions. *J. Phys. C*, 5:1921–1929, 1972.
- [79] J. W. Alexander and G. B. Briggs. On types of knotted curves. *Ann. of Math.*, 28(562), 1926–1927.
- [80] G. Gompper, T. Ihle, D.M. Kroll, and R.G. Winkler. Multi-Particle Collision Dynamics - a Particle-Based Mesoscale Simulation Approach to the Hydrodynamics of Complex Fluids. *Adv. Polym. Sci.*, 221:1–91, 2008.
- [81] J. Grotendorst, G. Sutmann, G. Gompper, and D. Marx. *Hierarchical Methods for Dynamics in Complex Molecular Systems Lecture Notes*, volume 10 of *IAS Series*. Forschungszentrum Jülich, Jülich, 2012.
- [82] L. Weiss, A. Nikoubashman, and C. N. Likos. Topology-Sensitive Microfluidic Filter for Polymers of Varying Stiffness. *ACS Macro Lett.*, 6:1426–1431, 2017.
- [83] T. Yamamoto and N. Masaoka. Numerical simulation of star polymers under shear flow using a coupling method of multiparticle collision dynamics and molecular dynamics. *Rheol. Acta*, 54:139–147, 2015.
- [84] G. S. Grest and K. Kremer. Molecular dynamics simulation for polymers in the presence of a heat bath. *Phys. Rev. A*, 33:3628–3631, 1986.
- [85] K. Kremer and G. S. Grest. Dynamics of entangled linear polymer melts: A molecular-dynamics simulation. *J. Chem. Phys.*, 92:5057–5086, 1990.
- [86] L. Verlet. Computer Experiments on Classical Fluids. I. Thermodynamical Properties of Lennard-Jones Molecules. *Phys. Rev.*, 159(1):98–103, 1967.
- [87] W. C. Swope, H. C. Andersen, P. H. Berens, and K. R. Wilson. A computer simulation method for the calculation of equilibrium constants for the formation of physical clusters of molecules: Application to small water clusters. *J. Chem. Phys.*, 76(1):637–649, 1982.
- [88] J. W. Alexander. Topological invariants of knots and links. *Trans. Amer. Math. Soc.*, 30:275–306, 1928.
- [89] Luca Tubiana, Enzo Orlandini, and Cristian Micheletti. Probing the Entanglement and Locating Knots in Ring Polymers: A Comparative Study of Different Arc Closure Schemes. *Prog. Theor. Phys. Suppl.*, 191:192–204, 12 2011.
- [90] J. L. White. Dynamics of viscoelastic fluids, melt fracture, and the rheology of fiber spinning. *J. Appl. Polym. Sci.*, 8:2339–2357, 1964.
- [91] John Nickolls, Ian Buck, Michael Garland, and Kevin Skadron. Scalable Parallel Programming with CUDA. *Queue*, 6:40–53, 03 2008.
- [92] E. Westphal, S.P. Singh, C.-C. Huang, G. Gompper, and R.G. Winkler. Multiparticle collision dynamics: GPU accelerated particle-based mesoscale hydrodynamic simulations. *CPC*, 185(2):495–503, 2014.
- [93] J. Rudnik and G. Gaspari. The asphericity of random walks. *J. Phys. A: Math. Gen.*, 19:L191–L193, 1986.
- [94] J.A. Aronovitz and D.R. Nelson. Universal features of polymer shapes. *J. Phys. (Paris)*, 47:1445–1456, 1986.
- [95] W. Chen, Y. Li, H. Zhao, L. Liu, J. Chen, and L. An. Conformations and dynamics of single flexible ring polymers in simple shear flow. *Polymer*, 64:93–99, 2015.
- [96] M. M. Denn and J. F. Morris. Rheology of non-Brownian suspensions. *Annu. Rev. Chem. Biomol. Eng.*, 5:203–228, 2014.